Interactive Virtual Endoscopy in Coronary Arteries based on Multi-Modality Fusion

Andreas Wahle,* *Senior Member, IEEE*, Mark E. Olszewski, *Student Member, IEEE*,
and Milan Sonka, *Fellow, IEEE*

Abstract— A novel approach for platform-independent virtual endoscopy in human coronary arteries is presented in this paper. It incorporates previously developed and validated methodology for multi-modality fusion of two X-ray angiographic images with pullback data from intravascular ultrasound (IVUS). These modalities pose inherently different challenges than those present in many tomographic modalities that provide parallel slices. The fusion process results in a three- or four-dimensional (3-D/4-D) model of a coronary artery, specifically of its lumen/plaque and media/adventitia surfaces. The model is used for comprehensive quantitative hemodynamic, morphologic, and functional analyses. The resulting quantitative indices are then used to supplement the model. Platform-independent visualization is achieved through the use of the ISO/IEC-standardized Virtual Reality Modeling Language (VRML). The visualization includes an endoscopic fly-through animation that enables the user to interactively select vessel location and fly-through speed, as well as to display image pixel data or quantification results in 3-D. The presented VRML virtual-endoscopy system is used in research studies of coronary atherosclerosis development, quantitative assessment of coronary morphology and function, and vascular interventions.

Index Terms— Coronary Atherosclerosis, Virtual Endoscopy, Virtual Reality Modeling Language, Intravascular Ultrasound, X-ray Angiography.

Special Issue on Virtual Endoscopy

Guest Editors:

- Jerome Z. Liang
- William E. Higgins
- Ronald M. Summers
- Hiro Yoshida

---

*A. Wahle is with The University of Iowa, Department of Electrical and Computer Engineering, Iowa City, IA 52242, USA (e-mail: a.wahle@ieee.org).

M. E. Olszewski and M. Sonka are with The University of Iowa, Department of Electrical and Computer Engineering, Iowa City, IA 52242, USA.

I. INTRODUCTION

COMPUTER-BASED visualization methods are gaining importance in the presentation of complex medical images and quantitative data. One of these techniques, *virtual endoscopy*, has been the foundation of a number of recently proposed systems. The major advantage of virtual endoscopic approaches is the visualization of tubular structures from the inside through a computer simulation derived from patient-specific anatomical data. Examples of typical applications of virtual endoscopy include virtual colonoscopy [1]–[4], virtual bronchoscopy [5], [6], and virtual angioscopy in the aorta [7] or hepatic vessels [8]. These methods are usually based on either X-ray computed tomography (CT) or magnetic resonance (MR) imaging modalities. In contrast, the established imaging modalities used for coronary arteries are X-ray angiography and intravascular ultrasound (IVUS) [9], which do not provide volumetric data in parallel slices. As a result, the arterial models obtained from these modalities require inherently different virtual-endoscopy methods than CT or MR. To the extent of our knowledge, there is no self-contained virtual-endoscopy system available that provides interactive and platform-independent visualization of coronary arteries derived from biplane angiography and IVUS data.

Coronary atherosclerosis involves progressive plaque development in the arteries, which is usually treated by percutaneous transluminal angioplasty (PTCA) and stenting. In coronary artery diseases, selective X-ray angiography is the method of choice for diagnosis and intervention. However, single-plane angiography allows only a limited analysis of the vessel lumen by quantitative coronary angiography [9], [10], and analyses from biplane angiography result in elliptical approximations of the lumen shape [11]. Attempts to achieve further refinement of the lumen shape based on X-ray densitometry have shown to be successful in larger vessels (e.g., iliac arteries [12] or ventricles [13]) and were also reported in coronary arteries [14], [15]. Substantially more detailed cross-sectional information (including plaque and vessel wall areas) can be obtained by IVUS, an established complement to X-ray angiography [16].

Conventional three-dimensional (3-D) reconstructions from IVUS stack the frames as acquired during the catheter pullback to form a straight volume, thus completely neglecting the vessel curvature. To overcome this limitation, we have developed a comprehensive system for *fusion* of the IVUS data with the pullback path determined from X-ray angiography, as previously documented in [17]–[20]. We have shown that the fusion of X-ray angiograms and IVUS images allows a recon-

struction of the morphologically realistic 3-D geometry of a coronary vessel (Fig. 1) and its four-dimensional (4-D, i.e., 3-D plus time) motion during a cardiac cycle [21]–[23]. Applications for these models are numerous and include: computational hemodynamics to calculate wall shear stress [24]–[28]; analyses to determine the correlation between vessel curvature and circumferential plaque distribution [29], [30]; and simulation of intravascular procedures, such as brachytherapy [31]–[33]. These applications all help understanding the mechanisms of arterial plaque development or treatment and their relationships to hemodynamics and morphology. Thorough investigation of these relationships is the major motivation for our ongoing research. This includes the determination of complex hemodynamic and morphologic indices as well as the interactive presentation of the results in an intuitive way. Virtual endoscopy provides a superior tool for visual evaluation of the vast amount of quantitative data within the context of the actual patient anatomy. In this way, associations can be made in ways that were not previously possible using standard charts and static models.

Three-dimensional virtual endoscopy from the fusion of IVUS and X-ray angiography is similar to 3-D virtual endoscopy from parallel CT or MR slices in that the correct vessel centerline and correct vessel surfaces must be found [2], [4]. However, IVUS images are acquired almost perpendicularly to the vessel centerline, thus simplifying surface generation and fly-through trajectory calculations. On the other hand, the 3-D reconstruction from biplane angiographic projections and the fusion with the IVUS data to obtain the 3-D contours along the catheter path is a complex task [17]–[20]. Our approach combines and integrates the 3-D fusion methodology with the quantitative evaluation to form a comprehensive 3-D/4-D model, and provides a new self-contained and platform-independent tool for visualization of the resulting model through virtual endoscopy. The ISO/IEC-standardized *Virtual Reality Modeling Language* (VRML) [34]–[37] has been used to describe the 3-D models and to present them interactively. To increase flexibility in interaction, VRML allows the encapsulation of Java or JavaScript nodes [34]. This concept was utilized to build a generic virtual-endoscopy VRML library [38] that, in general, can be applied to any 3-D data.

Section II describes the methodology developed to obtain and to visualize the 3-D model: the data acquisition and fusion processes; the representation of the IVUS pixel data in VRML; the inclusion of quantitative results from hemodynamic and morphologic analyses; the determination of the fly-through trajectory in the arterial model; and the graphical user interface, along with its implementation in VRML; as well as the patient population utilized for the presented in-vivo studies. Section III provides results from the underlying fusion and quantification components in two application examples, and details on the performance of the endoscopic-visualization system, followed by the discussion and conclusion in Sections IV, V.

II. METHODS

A schematic overview of the individual parts of the fusion, analysis, and visualization system is given in Figure 2. This paragraph will provide a short summary, whereas the following subsections present the individual components in more depth. The fusion subsystem, detailed in Fig. 3, generates a single 3-D model (or a set of 3-D models in the 4-D case [22]) derived from biplane angiography and intravascular ultrasound. It maps the 2-D frames into 3-D space along with the 3-D coordinates of the segmented contours. Quantitative analyses can be performed on these data by the respective subsystems, providing one or more values from quantitative measurements at each vertex point. These values are then used to supplement the 3-D model, thus to allow a point-to-point correspondence between any given border location and the respective hemodynamic and morphologic indices. The frames and contours are used to automatically create a VRML scene, with the results of the quantitative analyses included as a color coding of the generated 3-D surfaces. The colormap can be chosen individually and adapted non-linearly to any given range of quantification units. To facilitate virtual endoscopy on the reconstructed and annotated 3-D model (Figs. 4, 5), a fly-through path is calculated to describe the movement pattern of a virtual observer within the scene, and the VRML code is linked to a comprehensive VRML *External Prototype Library* [34], [35], [38]. Our library provides the necessary functionality for the endoscopic mode, including a graphical user interface for navigation through the vessel.

Subsections II-A to II-C describe the process of generating a spatial model of the coronary arteries, whereas subsections II-D to II-F present the details on the realization and the user interface of the virtual-endoscopy system as implemented through the developed VRML library. The patient data utilized for the in-vivo studies are introduced in subsection II-G.

A. Data Acquisition and Fusion Process

The image acquisition consists of two components: an IVUS pullback of up to 240 sec at 0.5 mm/sec constant motorized speed, and a pair of angiographic images. The angiograms are acquired with 50%-diluted contrast dye, showing both the IVUS catheter in its most distal location as well as the outline of the vessel lumen [17]–[20]. The angiographic imaging protocol ensures that ambiguities introduced by excessive foreshortening or vessel overlap are minimized in order to obtain an optimum 3-D reconstruction of the catheter path [39], [40]. During imaging, no manual interaction with either IVUS or angiographic devices is allowed to avoid distortions from table movement or catheter shifts. The subsequent fusion process is based on previously developed methodology [17], [18] and consists of the following sequence of tasks (Fig. 3):

1) acquire IVUS and angiographic data;
2) sort IVUS and angiographic data by the heart phase;
3) segment data for vessel and tissue structure;
4) determine 3-D location for each segmented point in each selected heart phase;
5) use resulting 3-D or 4-D data for quantitative analysis.

To obtain a correct model from in-vivo patient data, it is essential that the data are sorted correctly by the heart phase with respect to the electrocardiogram (ECG) [22]. The DICOM standard [41] has been used as an archiving medium, since it provides the means to store the ECG signal as well as acquisition parameters (imaging geometry, frame rate, and field of view)

along with the image data [9]. It has to be kept in mind that, due to the triggered acquisition during the continuous pullback, IVUS frames are only acquired at specific time instances during each heart cycle, thus the sampling along the vessel axis is rather sparse.

The catheter path and the outline of the vessel lumen are extracted semi-automatically from the angiograms, providing the pullback trajectory and a reference for the fusion process. The IVUS data are segmented to obtain the lumen/plaque and media/adventitia contours [19]. Well-established graph-search-based segmentation methods, which were fine-tuned for the specific image data, are used [9]. The fusion process itself consists of identifying the location of each IVUS frame in each phase, followed by the determination of the orientation of the frame in 3-D space in a two-step non-iterative statistical approach based on differential geometry [17], [18]. In the first step, the axial twisting of the catheter is determined using an analytical (Frenet-based) model, which provides the *relative* changes in orientation from frame to frame. In the second step, the overall *absolute* orientation of the frame set is determined by mapping the outline of the vessel with the contours of the IVUS frames in 3-D. The output of the fusion system consists of the 3-D catheter path, a 2-D to 3-D mapping for each IVUS frame, and 3-D tubular models for the two contours (Fig. 3). In the 4-D case, each component is generated for every selected heart phase. Sorting of the continuous IVUS pullback by heart phase results in 6–10 frame sets, each representing a single phase. The 3-D models are reconstructed individually per phase using the fusion system, and intermediate phases are interpolated using cubic splines, thus yielding the final 4-D model.

B. Modeling of the IVUS Pixel Data

Figure 5(a) shows a semi-transparent representation of the raw IVUS data that can be included in the scene. Considering that the pixel data from all frames can be represented as a volume, volume-rendering approaches could be used for visualization. For example, we have introduced the *Energy-Complement Projection* [42] for ray casting in IVUS data. However, a volume-rendering implementation in VRML and JavaScript would have had a negative impact on performance. The main reason is the lack of (or at least reduced) hardware acceleration for such an implementation. Therefore, the fully hardware-supported two-dimensional (2-D) texture-mapping capabilities of VRML were utilized to implement a 3-D texture-mapping approach. Similar approaches to render a 3-D volume as a set of 2-D surfaces have been reported before [43] and have been shown to perform better in terms of rendering speed than true volume-rendering approaches [44]. Each pixel is associated with its own opacity value, which can be directly encoded in the VRML *PixelTexture* node. Thus, the pixel data are represented as 2-D planes in 3-D space, modeling each IVUS frame and its texture-mapping information [38].

Pixel opacity is based on the location of the pixel within the image as well as its gray value. Structures not related to the vessel wall or plaque should not be visible. This is achieved by masking the image, which in the simplest case excludes an area defined by a fixed ring around the catheter location. A more sophisticated masking can be applied by using the IVUS segmentation information, thus excluding the lumen from being visible and removing any echoes beyond the external lamina. The excluded pixels are encoded with zero opacity (thus, full transparency) and allow an unobstructed view through the frame at the specified location. For the remaining data, a specifiable gray-value range $[v_{\min} \cdots v_{\max}]$ is mapped linearly to the opacity values $[0 \cdots 255]$ for each pixel. For example, a bright echo may indicate a calcification and would be encoded with a high opacity value. On the other hand, dark portions of the image may indicate the lumen of another vessel or other structures not providing an echo and would therefore have a lower opacity. Note that the masking of the image is for obtaining a better visualization result only, it does not affect performance since the number of pixels to be processed remains unchanged.

C. Hemodynamic and Morphologic Data

Once the 3-D model is created, it can be used to quantify hemodynamic parameters (such as local wall shear stress) and morphologic parameters (such as plaque thickness or volume and local curvature) in vessel segments between major branches. These parameters are highly relevant to determine the relationships between vessel geometry, wall-shear stresses, and the resulting plaque development. Since detailed descriptions of how these parameters are obtained were previously provided elsewhere [22], [23], [30], only a brief summary is given here.

For the determination of the wall shear stress, a finite-element mesh is created from the 3-D contour data, representing the vessel lumen. Structured radial and – more recently – unstructured tetrahedral meshes are used. For analyses performed at our institution, the U^2RANS [45] computational-fluid-dynamics system is utilized, which was developed at the University of Iowa Institute of Hydraulic Research and is suitable for moving-grid simulations in 4-D. Further analyses were performed in close collaboration with the Brigham & Women's Hospital and the Northeastern University in Boston, MA [27], [28]. The resulting shear stress data at the lumen/plaque interface are extracted and mapped onto the original lumen-contour data (Fig. 5).

Morphological analyses are used to correlate circumferential plaque distribution with vessel geometry (e.g., curvature). While the determination of the plaque thickness is straightforward, a local *curvature index* κ_{idx} has been defined that combines the magnitude of the local curvature with the circumferential position of a specific contour point [Fig. 6(a,b)]. Following the hypothesis that plaque tends to accumulate on the *inner* bend of a curved vessel (inner curvature) rather than on the *outer* bend (outer curvature), our aim was to identify the frequency of vessel regions for which high plaque accumulation coincides with locations at the inner curvature of the vessel and vice versa. These regions are marked in blue in Fig. 6(c).

The resulting data yield one or more values for each point of the reconstructed 3-D model. These values are used to build a colormap for visualization which, depending on the application, can either be defined per vessel or over a set of patients to allow inter-patient comparison. For each parameter (i.e., shear stress, curvature index, plaque thickness), a histogram is created over the set of vessels. The parameter values at the 2nd, 15th, 50th, 85th, and 98th percentiles are utilized to fit a piecewise cubic

function onto the histogram. A lookup table is generated for 256 value ranges based on this function. Then, the color scale of choice (rainbow, blue–red, grayscale, etc.) is applied to the lookup table, yielding the final color distribution.

D. Computation of the Fly-Through Trajectory

In VRML, the fly-through path has to be calculated as a sequence of viewpoints through the observed vessel. Each of those viewpoints is defined by a position and an orientation. The first subsection presents the general definition of the orientation parameter, which is represented by a rotation of the observer's local coordinate system around an arbitrary axis. The second subsection shows the actual determination of the axis and the angle to obtain an appropriate orientation of the observer within the vessel.

The remainder of this section uses the following notation: $\mathbf{R}$ indicates 3×3 rotation matrices, either by an angle α, β, γ around vectors $\vec{x}_e, \vec{y}_e, \vec{z}_e$ representing the x, y, z-axes in the Euclidean space; or by an angle φ around an arbitrary axis $\vec{r}$. Any point P_i of the fly-through trajectory is uniquely identified by a vector $\vec{p}_i = [x_i, y_i, z_i]$, where i is the frame index in the order of acquisition from distal to proximal. Vectors $\vec{x}_i, \vec{y}_i, \vec{z}_i$ represent the local viewing coordinate system associated with point P_i. All coordinate systems are right handed.

1) Rotations in VRML: Conventionally, 3-D rotations are expressed with reference to the three major axes in space, i.e.,

$$
\begin{aligned}
\mathbf{R}_x(\alpha) &= \begin{bmatrix} 1 & 0 & 0 \\ 0 & \cos\alpha & -\sin\alpha \\ 0 & \sin\alpha & \cos\alpha \end{bmatrix} \\[6pt]
\mathbf{R}_y(\beta) &= \begin{bmatrix} \cos\beta & 0 & \sin\beta \\ 0 & 1 & 0 \\ -\sin\beta & 0 & \cos\beta \end{bmatrix} \qquad (1) \\[6pt]
\mathbf{R}_z(\gamma) &= \begin{bmatrix} \cos\gamma & -\sin\gamma & 0 \\ \sin\gamma & \cos\gamma & 0 \\ 0 & 0 & 1 \end{bmatrix}
\end{aligned}
$$

In contrast, VRML uses a generalized definition with a single rotation $\mathbf{R}_r(\varphi)$ by an angle φ around an arbitrary axis r. This "axis-and-angle" definition is widely used in VRML and is also well-known from robotics [46]. Using the definitions in Eq. (1), $\mathbf{R}_r(\varphi)$ can be represented as a chain of five rotations:

$$
\begin{aligned}
\mathbf{R}_r(\varphi) &= \mathbf{R}_x(-\alpha)\,\mathbf{R}_y(\beta) \\
&\times \mathbf{R}_z(\varphi) \qquad\qquad (2) \\
&\times \mathbf{R}_y(-\beta)\,\mathbf{R}_x(\alpha)
\end{aligned}
$$

where the first two rotations align the r-axis with the z-axis by rotation around the x- and y-axes by α and β, respectively; the third component represents the actual rotation by φ, now around the z-axis; and the last two components are the inverses of the first two rotations to compensate for the alignment step. As shown in [46], α and β can be obtained directly from the $[r_x, r_y, r_z]$ components of $\vec{r}$, which is the unit vector defining the positive r-axis:

$$
\begin{aligned}
\sin\alpha &= \frac{r_y}{\sqrt{r_y{}^2 + r_z{}^2}} \\[6pt]
\cos\alpha &= \frac{r_z}{\sqrt{r_y{}^2 + r_z{}^2}}
\end{aligned} \qquad (3)
$$

$$
\begin{aligned}
\sin\beta &= r_x \\[6pt]
\cos\beta &= \sqrt{r_y{}^2 + r_z{}^2}
\end{aligned} \qquad (4)
$$

2) Calculation of the Viewpoints: The position and the orientation of a VRML *ViewPoint* node can be expressed as a triplet $(\vec{p}, \vec{r}, \varphi)$ containing a position vector $\vec{p}$, a rotation axis $\vec{r}$, and a rotation angle φ in a right-handed coordinate system. The initial viewing direction is along the negative z-axis (Fig. 7) [34], [35]. Thus, the problem of determining the orientation of an observer for a given path in $[x, y, z]$ coordinates is actually the reverse of the description in Section II-D.1.

For each point P_i of the trajectory, the respective $(\vec{p}_i, \vec{r}_i, \varphi_i)$ have to be calculated. The vectors $\vec{p}_i$ can be directly derived from either the catheter location for frame i (to follow the catheter path), or from the centroid of the segmented lumen contour (to follow the vessel centerline). The first method is the default and usually leads to a smoother animation due to the stiffness of the catheter. For the orientation, the rotation axis $\vec{r}_i$ and the angle φ_i are calculated as:

$$
\begin{aligned}
\vec{d}_i &= \vec{p}_{i+1} - \vec{p}_i \\
&= \left[(x_{i+1} - x_i), (y_{i+1} - y_i), (z_{i+1} - z_i) \right] \qquad (5) \\
&= [\, d_{x_i}, d_{y_i}, d_{z_i} \,]
\end{aligned}
$$

$$
-\vec{z}_i = \frac{\vec{d}_i}{\|\vec{d}_i\|} \qquad (6)
$$

$$
\begin{aligned}
\vec{r}_i &= \frac{-\vec{z}_e \times -\vec{z}_i}{\|-\vec{z}_e \times -\vec{z}_i\|} \qquad (7) \\[6pt]
&= \left[\left(\frac{d_{y_i}}{\sqrt{d_{x_i}{}^2 + d_{y_i}{}^2}} \right), \left(\frac{-d_{x_i}}{\sqrt{d_{x_i}{}^2 + d_{y_i}{}^2}} \right), 0 \right]
\end{aligned}
$$

$$
\cos\varphi_i = -\vec{z}_e \cdot -\vec{z}_i = -\left(\frac{d_{z_i}}{\|\vec{d}_i\|} \right) \qquad (8)
$$

where $\vec{p}_i$ and $\vec{p}_{i+1}$ are the position vectors of P_i and the next point P_{i+1} of the trajectory path; $\vec{d}_i$ is the direction vector from point P_i to P_{i+1}; $-\vec{z}_i$ is the desired viewpoint direction, with $-\vec{z}_e = [0, 0, -1]$ indicating the initial view (Fig. 8). Note that the z-component of $\vec{r}_i$ is always zero, thus the axis of rotation is in the x/y plane. This results from the inherent ambiguity of the axial orientation of an IVUS frame [17], [18]. The model described above does not consider the absolute orientation of the IVUS catheter in 3-D space and ignores the second angle in Eq. (2), thereby only modeling angle α in Eq. (3) with a constant β. Consequently, the definition of "up" in the image

will always be the same for each given viewing direction $-\vec{z}_i$. Combining Eqs. (2) and (7), the rotation axis $\vec{r}_i$ can also be defined as a rotation of the default VRML view-up direction $\vec{y}_e$ by an angle δ_i derived from α_i as follows:

$$
\begin{aligned}
\vec{r}_i &= \vec{y}_e \times \mathbf{R}_z(\delta_i) \\
\text{with} \quad \delta_i &= \alpha_i - \frac{\pi}{2} \\
\text{and} \quad \beta_i &= \frac{\pi}{2}
\end{aligned}
\tag{9}
$$

If it is desired that the fly-through trajectory accurately represents the absolute orientation of the IVUS catheter during pullback, the set of equations would have to be extended by an axial correction angle around $-\vec{z}_i$ to align the local coordinate system with the frame orientation determined during the fusion step (Sec. II-A).

A special case exists at the end of the fly-through trajectory, because there is no point P_{i+1} for the final point P_i with $i = (n-1)$ in a set of n points $\{P_0 \cdots P_{n-1}\}$; therefore,

$$
\begin{aligned}
\vec{r}_{n-1} &= \vec{r}_{n-2} \\
\varphi_{n-1} &= \varphi_{n-2}
\end{aligned}
\tag{10}
$$

are assumed, thus yielding a viewpoint definition for all P_i.

E. Three-Dimensional Graphical User Interface

After startup, the initial scene shows the vessel in a frontal view, and indicates the location of the endoscopic observer by a pyramid representing the observer's eye and viewing direction (Fig. 4). The user can switch between several different representations (e.g., just the semi-transparent IVUS frames in their correct orientations and locations, the lumen surface with or without the frames, or the surface with the color-coded quantification results) and can enter or exit the endoscopic view at any time.

While the initial viewpoint allows the handling of the scene as with any other VRML world, the endoscopic view requires more sophisticated features for navigation. An automated fly-through with variable speed and an arbitrary positioning within the vessel cannot be accomplished by the standard VRML animation nodes alone. Another design challenge is the presentation of the control panel itself, which should be available on demand, but must neither obstruct any vessel features when not needed, nor reduce the viewport for the scene.

We solved the control-panel problem by putting the panel within the endoscopic scene itself, attached to the virtual observer similarly to how eyeglasses would fit a real observer. Figure 9 depicts the appearance of the control panel when activated. Since the control panel moves in 3-D with the observer, it seems to be at a constant location from the user's point of view. The control panel is switched off by default, but can be activated by clicking on an invisible object in the scene (proxy shape) directly in front of the observer. A nested set of these (invisible) proxy shapes is placed in front of the observer, as Fig. 10 shows from a side view. Note that only those 3-D shapes which allow the manipulation of the scene are visible, and only

if and when desired by the user. Once the user moves the mouse outside of the central proxy shape to the outer one, the control panel disappears to allow an unobstructed view of the scene.

The control panel provides the following features to manipulate the scene (Fig. 9):

- With the PROX and DIST buttons, the viewing orientation of the observer can be changed to the proximal direction or to distal direction, respectively.
- The upper slider indicates the *speed* of the virtual observer in either the proximal or the distal direction; the observer does not move when the sphere is in the center. Clicking the STOP button above the slider stops any motion of the virtual observer.
- The lower slider indicates the current *location* of the virtual observer; it moves whenever the observer is moving, or it can be dragged directly to any location.
- The IVUS button switches the panel into a different mode, where the IVUS frame corresponding to the current location is shown; with two arrows buttons, the user can move in either the proximal or the distal directions on a frame-by-frame basis.
- The VIEW button switches the vessel representation, as was described above.
- The EXIT button will change the scene to a viewpoint outside of the vessel and will leave the endoscopic mode, reactivating the browser's control panel.

F. Generic VRML External Prototype Library

The right-hand side of Fig. 2 shows a hierarchy of several VRML worlds. To allow efficient reuse of common VRML and JavaScript code for all generated scenes, and to effectively minimize the size of the VRML files, a generic *External Prototype Library* was developed, the mechanism for which is defined in the standard [34], [35]. Our prototype library is shared by all endoscopic scenes. The VRML worlds are created semi-automatically from the 3-D frames and contours generated by the fusion system, and the worlds are cross-linked with the prototype library. The main effort by the user is the specification of the visualization options (e.g., which combinations of representations are desired, and which colormap is applied to which quantitative parameter). While the automatically generated VRML worlds describe the vessel geometry and fly-through path, the necessary logic and controls are implemented in the prototype library. A detailed description of this library and the VRML worlds is given in [38]. The following list summarizes the core functions of the five different node prototypes that were implemented in the library:

- *EndoscopyInterpolator:* defines and controls the fly-through trajectory by combining the VRML *PositionInterpolator* and *OrientationInterpolator* nodes. The location can either be explicitly set using the slider of the control panel from the *EndoscopyObserver* node, or the internal *TimeSensor* can be activated for a continuous fly-through scene.
- *EndoscopyObserver:* provides the 3-D user interface and shares the same coordinate system as the endoscopic *Viewpoint* node, which in turn is manipulated by the *En-*

doscopyInterpolator node. Together, the *EndoscopyObserver* and *EndoscopyInterpolator* nodes provide the core functionality for the fly-through animation and control.

- *EndoscopyNavigator:* takes care of the actions necessary when entering the endoscopic mode: The lighting scheme is changed from the directional headlight to a point light at the location of the observer, and the browser controls are switched off to prevent interference with the controls of the *EndoscopyObserver* node.
- *EndoscopyObjSwitch:* alternates between the different vessel representations, either requested by clicking on the currently visible VRML object or the VIEW button of the endoscopic panel.
- *EndoscopyObjInclude:* exists for each external static VRML world (e.g., IVUS frames, vessel wall surfaces, color-coded surfaces). It implements an extension of the VRML *Inline* node by enabling the switching of its visibility.

G. In-vivo Patient Data

In-vivo data were acquired from patients undergoing routine diagnosis and intervention at the University of Iowa Hospitals and Clinics; at Brigham & Women's Hospital in Boston, MA; at the University of Chicago, IL; and at the University of Essen in Germany. At the University of Iowa, a biplane Philips Integris BH–5000 device (Philips Medical Systems, Best, The Netherlands) was utilized. Angiographic data were exported in DICOM format. IVUS data were acquired with a ClearView ultrasound system (Boston Scientific, Boston, MA) using 30- or 40-MHz rotating-transducer catheters, recorded on and digitized from S–VHS tape. Motorized continuous pullback was used at the speed of 0.5 mm/sec. Similar setups were used at the collaborating sites, with single-plane angiographic systems in Boston and Chicago. To date, in-vivo data from a total of 62 patients were acquired and used in this ongoing study.

Complete end-diastolic 3-D analyses (including fusion, calculation of wall shear stress, and morphologic analysis for plaque thickness and local curvature) currently exist for 37 coronary segments ranging 41.9–122.5 mm in pullback length (14 right coronary arteries, 13 left anterior descending arteries, and 10 left circumflex arteries). Four-dimensional models were generated in three pullbacks, and eight patients were selected for an intravascular-brachytherapy study [33].

III. RESULTS

A. Studies of Hemodynamic Effects of Coronary Interventions

In the set of 62 patients available thus far, 12 patients underwent IVUS imaging both prior and after PTCA and stenting. An example is shown in Fig. 11 with a pullback length of 54.8 mm. Of special interest in these patients are the hemodynamic changes between the pre- and post-interventional vessel geometries. As can be seen in Fig. 11(a), different physiological parameters may have to be taken into account, in this case a reduced heart rate and corresponding changes in blood pressure after the intervention. The lower blood velocity resulted in overall lower wall shear stress,

making a direct comparison of the two shear-stress distributions difficult. Instead of using standardized input parameters for the computational-hemodynamics calculations, the color maps were normalized as described in Section II-C. In the pre-interventional case, the set of automatically determined percentile values was 1.74, 5.96, 14.40, 21.57, 34.40 Pa as compared to 2.08, 3.66, 6.20, 8.84, 11.88 Pa for the post-interventional case. The resulting color distribution shown in Fig. 11(b) now allows a direct comparison of the shear-stress changes caused by the intervention. Beyond the determination of effects of interventions on the wall shear stress, the resulting 3-D models have also been utilized to determine redistribution and compression of plaque during PTCA and stenting. While this study is still ongoing, preliminary results indicate that the redistribution of plaque can be identified by volumetric changes within the plaque segments, and compression by a comparison of the geometrically correct overall 3-D volume prior to and after the intervention.

B. Correlation between Plaque and Curvature

For the 37 vessel segments completed thus far, circumferential plaque distribution and curvature indices were calculated as described in Section II-C to verify the hypothesis that plaque tends to accumulate along the *inner* curvatures rather than along the *outer* curvatures. Four regions R_{ai}, R_{ao}, R_{bi}, and R_{bo} were defined, distinguishing circumferentially-considered "above average" plaque thickness (a) from "below average" plaque thickness (b), as well as the "inner curvature" (i) from the "outer curvature" (o) of the vessel wall. Satisfying the inequality $\|R_{ai}+R_{bo}\| \geq \|R_{ao}+R_{bi}\|$ indicates that more plaque is accumulating along the inner curvature as compared to the outer curvature. As illustrated in Figs. 6(c) and 12, a threshold was applied to exclude regions of low curvature from the results, thus avoiding the inclusion of noise. For the threshold, 12 different values were empirically selected ranging from 2.31 to 22.94°/cm, resulting in 10.2–78.3% of circumferential locations being excluded. In 29 of the 37 vessel segments, the hypothesis held for at least half of the thresholds (i.e., the inequality was satisfied for 6 or more of the 12 sets of regions R_{ai}, R_{ao}, R_{bi}, and R_{bo}). In only 6 of the 37 vessel segments the inequality did not hold for *any* of the applied thresholds. The comparison of the region assignments in calculations that included stented areas vs. those in which stented areas were excluded showed no statistical difference ($p > 0.20$ for all thresholds ≥ 6.86°/cm).

C. Performance Assessments

The accuracy of the endoscopic model depends primarily on the underlying fusion and quantification techniques, and also relies on the numerical accuracy of the hardware used and the display capabilities of the browser. While the validation of the overall fusion system was performed in phantoms and in-vitro studies on pig hearts [17], only performance and visual accuracy could be analyzed for the virtual-endoscopy system itself. VRML and JavaScript *describe* the 3-D objects in space and their interaction with each other and with the user, whereas the

actual presentation depends on the browser employed. The in-vivo right coronary artery in the end-diastolic phase shown in Fig. 4 included 172 ECG-gated frames for the VRML modeling. The resulting scene required approximately 141 MB of disk space, the bulk of which resulted from the ASCII-text encoding of the pixel data as defined by the VRML standard. With white spaces minimized, 731,442 characters of VRML code were generated for each 384×384-pixel IVUS frame on average. Since all the data are loaded into main memory when the VRML browser is started, and since browsers are usually Open-GL based, performance is mainly dependent on the hardware employed. Using the Cosmo-Player 2.1 browser plug-in (Cosmo Software, Computer Associates International Inc., Islandia, NY), the loading time for the scene described above is about 24 sec on a dual-processor 2 GHz AMD Athlon PC (Advanced Micro Devices Inc., Sunnyvale, CA) with 3.5 GB of main memory and an ATI Radeon 9700 Pro (ATI Technologies, Markham, OT, Canada) graphics card with 128 MB of video memory. Navigation can be performed in real time after the scene has been loaded. In our experience, most currently available graphics cards offer acceptable performance. The desktop configuration with the least performance tested, a 768 MB, 600 MHz-Pentium III with a 32 MB Diamond Viper V770D Ultra AGP graphics card (Diamond Multimedia Systems, Chatsworth, CA), still showed good real-time performance with IVUS texture-mapping applied.

IV. DISCUSSION

The presented approach combines and integrates methodology for 3-D fusion of coronary artery image data from X-ray angiography and IVUS, along with quantitative analyses. While parts of the methodology have been developed and validated previously as independent blocks, the novelty introduced here is the overall synthesis of geometric reconstruction, true 3-D quantitative analyses, the generation of new complex indices such as the correlation of circumferential plaque distribution and local curvature, as well as the interactive presentation of the models to convey the analysis results to the observer.

The visualization in VRML, along with the endoscopic mode, allows interactive evaluation of normal and diseased vessel segments by directly relating the geometry of a vessel with its 3-D morphologic and hemodynamic data. The process of obtaining an endoscopic scene from the 3-D fusion result is straightforward, highly automated, requires only the selection of a few visualization options, and needs only seconds for the automated generation of the VRML code. We developed a new generic prototype library that extends the capabilities of the user to navigate within the vessel. It also allows to better manipulate the automated fly-through animation as compared to the regular controls provided by the VRML browser. The possibility to switch between several different vessel representations and to include or exclude pixel data or color-coded quantification results arbitrarily within the endoscopic scene allows for a highly flexible presentation of the scene that takes individual preferences into account. 3-D texture mapping was preferred over true volume rendering, mainly because this mode is best supported by the hardware acceleration of common VRML browsers and their frequently underlying implementation in Open-GL. Other reasons include the need to work with highly anisotropic data (due to the sparse sampling along the vessel axis) and the need to deal with non-parallel slices. Both of these issues make a ray-casting approach more challenging than the selected texture mapping.

Despite the potentially large amount of data to be processed by the visualization system, all equipment used to generate the aforementioned results were "off-the-shelf" products. Possible alternatives to VRML include either a direct implementation in Open-GL or the *Visualization Toolkit* (VTK) [47]. The major advantage of VRML is its platform independence, whereas Open-GL or VTK require construction of a platform-specific visualization software, without necessarily providing a higher performance. Since VRML is essentially a 3-D description language, it facilitates a direct visualization of the scene in immersive environments (e.g., CAVE [48]). However, support of the implemented JavaScript control mechanisms depend on the specifics of the chosen environment and may need adjustment to make full use of the sensors and controls in immersive environments.

As briefly discussed in Section II-D.2, the current computation of the fly-through trajectory does not align the view-up vector of the virtual observer with those of the IVUS images. While it is straightforward to calculate and consider this additional axial rotation, such approach would be more confusing than helpful. Assuming, e.g., a segment of helical nature, the view would rotate axially due to the twisting of the catheter while following the trajectory. This may confuse the user's sense of direction more than the selected viewing orientation that maintains a stable view-up direction in 3-D world coordinates. Furthermore, if the trajectory is based on the vessel centerline rather than the pullback, the effects of parallax may be added. In summary, it seemed appropriate to implement the viewing orientation as presented here.

The system is currently restricted to a *single* fly-through trajectory, which may be considered a limitation. However, usually only single vessel segments are subjected to the reconstruction and the subsequent quantification steps. Branches are currently excluded from both hemodynamic and morphologic analyses. Multiple branches are difficult to obtain in a clinical setting anyway since only segments undergoing intervention are usually imaged to limit the duration of the invasive procedure and the possibility of associated complications. In theory, the virtual-endoscopy system could be expanded to consider multiple fly-through trajectories, thus allowing the user to follow different branches. The main challenge in such an approach would be merging models from multiple pullbacks into a single, larger model.

An extension of the endoscopic mode into 4-D would be desirable, as already done for non-endoscopic VRML worlds [22]. This would require an extension of the *EndoscopyInterpolator* and *EndoscopyObserver* nodes to allow real-time modification of the fly-through trajectory along with the animation of the moving vessel. As the vessel cycles through the heart phases, care has to be taken that the endoscopic observer remains within the vessel and that the viewing direction is adjusted accordingly. In general, the same technique would apply as discussed before

with respect to branches (i.e., multiple fly-through trajectories would be calculated for each time instance and then automatically cycled through). The trajectories could be determined automatically while performing the spline-based interpolation of the vessel contours. The necessary extension of the control panel would imply additional sliders and buttons to navigate between the heart phases. Their design could follow those of the sliders for the location (i.e., providing a slider for the current time instance along the cardiac cycle, and another one determining the speed of the cycling through the phases).

Our previously developed fusion systems based on biplane angiography and IVUS data provides a well-established basis for quantitative analyses. Computer simulations utilizing piecewise linear and continuously curved 3-D models, along with in-vitro validation showed a good accuracy of the fusion system [17] despite artifactual distortions caused by friction between the rotating catheter core and the sheath, especially in strongly curved vessels, and other inherent problems of IVUS imaging (e.g., shadowing due to calcifications). Phantom validation and computer simulations were also performed for the wall shear stress [22] and volumetric [23] measurements, demonstrating a good agreement with their respective analytical models and published gold standards. A study analyzing the reproducibility of the multi-modality fusions and the hemodynamic analyses based on multiple pullbacks in 10 coronary arteries has been performed [28].

V. Conclusion

Data fusion of biplane angiography and intravascular ultrasound, combined with computational hemodynamics, morphologic analyses, and interactive 3-D visualization offers an abundance of information that can be used for diagnosis and evaluation of coronary interventions. Our virtual-endoscopy approach offers a better access to these data. Platform-independent distribution and visualization are ensured through the use of the standardized VRML 3-D modeling language. The combination of VRML prototypes with JavaScript nodes allows the implementation of a comprehensive graphical user interface for the endoscopic mode, while the default browser controls are used in all other views. The 3-D control panel is included in the scene on demand without obstructing the view when not in use. The panel allows interaction with the scene in real time. The presented VRML-based virtual-endoscopy approach enables a better evaluation of the reconstructed and calculated data in a local or global context.

Acknowledgments

References

[1] G. Wang, E. G. McFarland, B. P. Brown, and M. W. Vannier, "Gastrointestinal tract unraveling with curved cross sections," *IEEE Transactions on Medical Imaging*, vol. 17, no. 2, pp. 318–322, Apr. 1998.

[2] Y. Samara, M. Fiebich, A. H. Dachman, J. K. Kuniyoshi, K. Doi, and K. R. Hoffmann, "Automated calculation of the centerline of the human colon on CT images," *Academic Radiology*, vol. 6, no. 6, pp. 352–359, June 1999.

[3] R. M. Summers, A. K. Hara, W. Luboldt, and C. D. Johnson, "Computed tomographic and magnetic resonance colonography: Summary of progress from 1995 to 2000," *Current Problems in Diagnostic Radiology*, vol. 30, no. 5, pp. 147–167, Sept./Oct. 2001.

[4] M. Wan, Z. Liang, Q. Ke, L. Hong, I. Bitter, and A. Kaufman, "Automatic centerline extraction for virtual colonoscopy," *IEEE Transactions on Medical Imaging*, vol. 21, no. 12, pp. 1450–1460, Dec. 2002.

[5] K. Mori, J. I. Hasegawa, Y. Suenaga, and J. I. Toriwaki, "Automated anatomical labeling of the bronchial branch and its application to the virtual bronchoscopy system," *IEEE Transactions on Medical Imaging*, vol. 19, no. 2, pp. 103–114, Feb. 2000.

[6] R. D. Swift, A. P. Kiraly, A. J. Sherbondy, A. L. Austin, E. A. Hoffman, G. McLennan, and W. E. Higgins, "Automatic axis generation for virtual bronchoscopic assessment of major airway obstructions," *Computerized Medical Imaging and Graphics*, vol. 26, no. 2, pp. 103–118, Mar./Apr. 2002.

[7] J. Beier, T. Diebold, H. Vehse, G. Biamino, E. Fleck, and R. Felix, "Virtual endoscopy in the assessment of implanted aortic stents," in *Computer Assisted Radiology and Surgery (CAR '97)*, H. U. Lemke, M. W. Vannier, and K. Inamura, eds., vol. 1134 of *Excerpta Medica International Congress Series*, Amsterdam, pp. 183–188, Elsevier, 1997.

[8] J. Beier, T. Vogl, T. Rohlfing, D. Strahlendorf, N. Hidajat, and R. Felix, "Virtual endoscopy in the CT-based assessment and control of TIPS (transjugular intrahepatic portosystemic shunt)," in *Computer Assisted Radiology and Surgery (CARS '99)*, H. U. Lemke, M. W. Vannier, K. Inamura, and A. G. Farman, eds., vol. 1191 of *Excerpta Medica International Congress Series*, Amsterdam, pp. 181–185, Elsevier, 1999.

[9] J. H. C. Reiber, G. Koning, J. Dijkstra, A. Wahle, B. Goedhart, F. H. Sheehan, and M. Sonka, "Angiography and intravascular ultrasound," in *Handbook of Medical Imaging — Volume 2: Medical Image Processing and Analysis*, M. Sonka and J. M. Fitzpatrick, eds., Bellingham WA, pp. 711–808, SPIE Press, 2000.

[10] B. G. Brown, P. Simpson, J. T. Dodge, E. L. Bolson, and H. T. Dodge, "Quantitative and qualitative coronary arteriography," in *Quantitative Coronary Arteriography*, J. H. C. Reiber and P. W. Serruys, eds., vol. 117 of *Developments in Cardiovascular Medicine*, Dordrecht, pp. 3–21, Kluwer, 1991.

[11] A. Wahle, E. Wellnhofer, I. Mugaragu, H. U. Sauer, H. Oswald, and E. Fleck, "Assessment of diffuse coronary artery disease by quantitative analysis of coronary morphology based upon 3-D reconstruction from biplane angiograms," *IEEE Transactions on Medical Imaging*, vol. 14, no. 2, pp. 230–241, June 1995.

[12] C. Pellot, A. Herment, M. Sigelle, P. Horain, H. Maître, and P. Peronneau, "A 3D reconstruction of vascular structures from two X-ray angiograms using an adapted simulated annealing algorithm," *IEEE Transactions on Medical Imaging*, vol. 13, no. 1, pp. 48–60, Mar. 1994.

[13] G. P. M. Prause and D. G. W. Onnasch, "Binary reconstruction of the heart chambers from biplane angiographic image sequences," *IEEE Transactions on Medical Imaging*, vol. 15, no. 4, pp. 532–546, Aug. 1996.

[14] J. H. C. Reiber, J. J. Gerbrands, G. J. Troost, C. J. Kooijman, and C. H. Slump, "3-D reconstruction of coronary arterial segments from two projections," in *Digital Imaging in Cardiovascular Radiology*, P. H. Heintzen and R. Brennecke, eds., Stuttgart/New York, pp. 151–163, Thieme, 1982/83.

[15] Y. Bao, H. Oswald, and E. Fleck, "The pyramid structure and its application to binary image reconstruction from two projections," in *Proc. International Conference on Acoustics, Speech, and Signal Processing (ICASSP-90)*, vol. 4, Piscataway NJ, pp. 1845–1848, IEEE Press, 1990.

[16] C. von Birgelen, E. A. de Vrey, G. S. Mintz, A. Nicosia, N. Bruining, W. Li, C. J. Slager, J. R. T. C. Roelandt, P. W. Serruys, and P. J. de Feyter, "ECG-gated three-dimensional intravascular ultrasound: Feasibility and reproducibility of the automated analysis of coronary lumen and atherosclerotic plaque dimensions in humans," *Circulation*, vol. 96, no. 9, pp. 2944–2952, Nov. 1997.

[17] A. Wahle, G. P. M. Prause, S. C. DeJong, and M. Sonka, "Geometrically correct 3-D reconstruction of intravascular ultrasound images by fusion with biplane angiography — methods and validation," *IEEE Transactions on Medical Imaging*, vol. 18, no. 8, pp. 686–699, Aug. 1999.

[18] A. Wahle, G. P. M. Prause, C. von Birgelen, R. Erbel, and M. Sonka, "Fusion of angiography and intravascular ultrasound in-vivo: Establishing the absolute 3-D frame orientation," *IEEE Transactions on Biomedical Engineering*, vol. 46, no. 10, pp. 1176–1180, Oct. 1999.

[19] A. Wahle, S. C. Mitchell, M. E. Olszewski, R. M. Long, and M. Sonka, "Accurate visualization and quantification of coronary vasculature by 3-D/4-D fusion from biplane angiography and intravascular ultrasound," in *European Biomedical Optics Week (EBiOS 2000): Biomonitoring and Endoscopy Technologies*, I. Gannot, Y. V. Gulyaev, T. G. Papazoglou, and C. F. P. van Swol, eds., vol. 4158, Bellingham WA, pp. 144–155, SPIE Europto, 2000/2001.

[20] M. E. Olszewski, A. Wahle, R. Medina, S. C. Mitchell, and M. Sonka, "Integrated system for quantitative analysis of coronary plaque via data fusion of biplane angiography and intravascular ultrasound," in *Computer Assisted Radiology and Surgery (CARS 2003)*, H. U. Lemke, K. Inamura, M. W. Vannier, A. G. Farman, K. Doi, and J. H. C. Reiber, eds., vol. 1256 of *Excerpta Medica International Congress Series*, Amsterdam, pp. 1117–1122, Elsevier, 2003.

[21] M. E. Olszewski, R. M. Long, S. C. Mitchell, A. Wahle, and M. Sonka, "Quantitative measurements in geometrically correct representation of coronary vessels in 3-D and 4-D," in *Proc. 4th IEEE Southwest Symposium on Image Analysis and Interpretation*, Los Alamitos CA, pp. 259–263, IEEE-CS Press, 2000.

[22] A. Wahle, S. C. Mitchell, S. D. Ramaswamy, K. B. Chandran, and M. Sonka, "Four-dimensional coronary morphology and computational hemodynamics," in *Medical Imaging 2001: Image Processing*, M. Sonka and K. M. Hanson, eds., vol. 4322, Bellingham WA, pp. 743–754, SPIE Proceedings, 2001.

[23] R. Medina, A. Wahle, M. E. Olszewski, and M. Sonka, "Three methods for accurate quantification of plaque volume in coronary arteries," *International Journal of Cardiovascular Imaging*, vol. 19, no. 4, pp. 301–311, Aug. 2003.

[24] C. M. Gibson, L. Diaz, K. Kandarpa, F. M. Sacks, R. C. Pasternak, T. Sandor, C. L. Feldman, and P. H. Stone, "Relation of vessel wall shear stress to atherosclerosis progression in human coronary arteries," *Arteriosclerosis and Thrombosis*, vol. 13, no. 2, pp. 310–315, Feb. 1993.

[25] K. B. Chandran, M. J. Vonesh, A. Roy, S. Greenfield, B. Kane, R. Greene, and D. D. McPherson, "Computation of vascular flow dynamics from intravascular ultrasound images," *Medical Engineering and Physics*, vol. 18, no. 4, pp. 295–304, June 1996.

[26] R. Krams, J. J. Wentzel, J. A. F. Oomen, R. Vinke, J. C. H. Schuurbiers, P. J. de Feyter, P. W. Serruys, and C. J. Slager, "Evaluation of endothelial shear stress and 3-D geometry as factors determining the development of atherosclerosis and remodeling in human coronary arteries in-vivo; combining 3-D reconstruction from angiography and IVUS (ANGUS) with computational fluid dynamics," *Arteriosclerosis, Thrombosis and Vascular Biology*, vol. 17, no. 10, pp. 2061–2065, Oct. 1997.

[27] P. H. Stone, A. Ü. Coşkun, S. Kinlay, M. E. Clark, M. Sonka, A. Wahle, O. J. Ilegbusi, Y. Yeghiazarians, J. J. Popma, J. Orav, R. E. Kuntz, and C. L. Feldman, "Effect of endothelial shear stress on the progression of coronary artery disease, vascular remodeling, and in-stent restenosis in man; in-vivo 6-month followup study," *Circulation*, vol. 108, no. 4, pp. 438–444, July 2003.

[28] A. Ü. Coşkun, Y. Yeghiazarians, S. Kinlay, M. E. Clark, O. J. Ilegbusi, A. Wahle, M. Sonka, J. J. Popma, R. E. Kuntz, C. L. Feldman, and P. H. Stone, "Reproducibility of coronary lumen, plaque, and vessel wall reconstruction and of endothelial shear stress measurements in-vivo in humans," *Catheterization and Cardiovascular Interventions*, vol. 60, no. 1, pp. 67–78, Sept. 2003.

[29] M. H. Friedman, P. B. Baker, Z. Ding, and B. D. Kuban, "Relationship between the geometry and quantitative morphology of the left anterior descending coronary artery," *Atherosclerosis*, vol. 125, no. 2, pp. 183–192, Sept. 1996.

[30] A. Wahle, R. Medina, K. C. Braddy, J. M. Fox, T. M. H. Brennan, J. J. Lopez, J. D. Rossen, and M. Sonka, "Impact of local vessel curvature on the circumferential plaque distribution in coronary arteries," in *Medical Imaging 2003: Physiology and Function: Methods, Systems, and Applications*, A. V. Clough and A. A. Amini, eds., vol. 5031, Bellingham WA, pp. 204–213, SPIE Proceedings, 2003.

[31] R. A. Fox, "Intravascular brachytherapy of the coronary arteries," *Physics in Medicine and Biology*, vol. 47, no. 4, pp. R1–R30, Feb. 2002.

[32] G. Koning, J. C. Tuinenburg, E. Hekking, J. Peelen, A. van Weert, D. Bergkamp, B. Goedhart, and J. H. C. Reiber, "A novel measurement technique to assess the effects of coronary brachytherapy in clinical trials," *IEEE Transactions on Medical Imaging*, vol. 21, no. 10, pp. 1254–1263, Oct. 2002.

[33] A. Wahle, J. J. Lopez, E. C. Pennington, S. L. Meeks, K. C. Braddy, J. M. Fox, T. M. H. Brennan, J. M. Buatti, J. D. Rossen, and M. Sonka, "Effects of vessel geometry and catheter position on dose delivery in intracoronary brachytherapy," *IEEE Transactions on Biomedical Engineering*, vol. 50, no. 11, pp. 1286–1295, Nov. 2003.

[34] A. L. Ames, D. R. Nadeau, and J. L. Moreland, *The VRML 2.0 Sourcebook*. New York: John Wiley and Sons, 2nd ed., 1997.

[35] ISO/IEC 14772, "Information technology — computer graphics and image processing — the virtual reality modeling language." International Organization for Standardization, Geneva CH, 1998.

[36] G. Taubin, W. P. Horn, F. Lazarus, and J. Rossignac, "Geometry coding and VRML," *IEEE Proceedings*, vol. 86, no. 6, pp. 1228–1243, June 1998.

[37] D. R. Nadeau, "Tutorial: Building virtual worlds with VRML," *IEEE Computer Graphics and Applications*, vol. 19, no. 2, pp. 18–29, Mar./Apr. 1999.

[38] A. Wahle, S. C. Mitchell, S. D. Ramaswamy, K. B. Chandran, and M. Sonka, "Virtual angioscopy in human coronary arteries with visualization of computational hemodynamics," in *Medical Imaging 2001: Physiology and Function from Multidimensional Images*, C. Chen and A. V. Clough, eds., vol. 4321, Bellingham WA, pp. 32–43, SPIE Proceedings, 2001.

[39] U. Solzbach, U. Oser, M. R. Rombach, H. Wollschläger, and H. Just, "Optimum angiographic visualization of coronary segments using computer-aided 3D-reconstruction from biplane views," *Computers and Biomedical Research*, vol. 27, no. 3, pp. 178–198, June 1994.

[40] S. Y. J. Chen and J. D. Carroll, "3-D reconstruction of coronary arterial tree to optimize angiographic visualization," *IEEE Transactions on Medical Imaging*, vol. 19, no. 4, pp. 318–336, Apr. 2000.

[41] NEMA PS3.1-16, "Digital imaging and communications in medicine (DICOM 3.0)." National Electrical Manufacturers Association, Rosslyn VA, 1993-2003.

[42] A. Wahle, S. C. Mitchell, C. von Birgelen, R. Erbel, and M. Sonka, "Onsite 3-D reconstruction and visualization of intravascular ultrasound based upon fusion with biplane angiography," in *Computer Assisted Radiology and Surgery (CARS '99)*, H. U. Lemke, M. W. Vannier, K. Inamura, and A. G. Farman, eds., vol. 1191 of *Excerpta Medica International Congress Series*, Amsterdam, pp. 56–60, Elsevier, 1999.

[43] B. Cabral, N. Cam, and J. Foran, "Accelerated volume rendering and tomographic reconstruction using texture mapping hardware," in *Proc. 1994 IEEE/ACM-SIGGRAPH Symposium on Volume Visualization*, New York, pp. 91–98, ACM Press, 1994.

[44] M. Meißner, J. Huang, D. Bartz, K. Müller, and R. Crawfis, "A practical evaluation of popular volume rendering algorithms," in *Proc. 2000 IEEE/ACM-SIGGRAPH Symposium on Volume Visualization*, New York, pp. 81–90, ACM Press, 2000.

[45] Y. G. Lai and A. J. Przekwas, "A finite-volume method for fluid flow simulations with moving boundaries," *Computational Fluid Dynamics*, vol. 2, pp. 19–40, 1994.

[46] K. S. Fu, R. C. Gonzalez, and C. S. G. Lee, *Robotics: Control, Sensing, Vision, and Intelligence*. CAD/CAM Robotics and Computer Vision, New York: McGraw-Hill, 1987.

[47] W. J. Schroeder, L. S. Avila, and W. Hoffman, "Visualizing with VTK: A tutorial," *IEEE Computer Graphics and Applications*, vol. 20, no. 5, pp. 20–27, Sept./Oct. 2000.

[48] C. Cruz-Neira, D. J. Sandin, T. A. DeFanti, R. V. Kenyon, and J. C. Hart, "The CAVE — audio visual experience automatic virtual environment," *Communications of the ACM*, vol. 35, no. 6, pp. 64–72, June 1992.
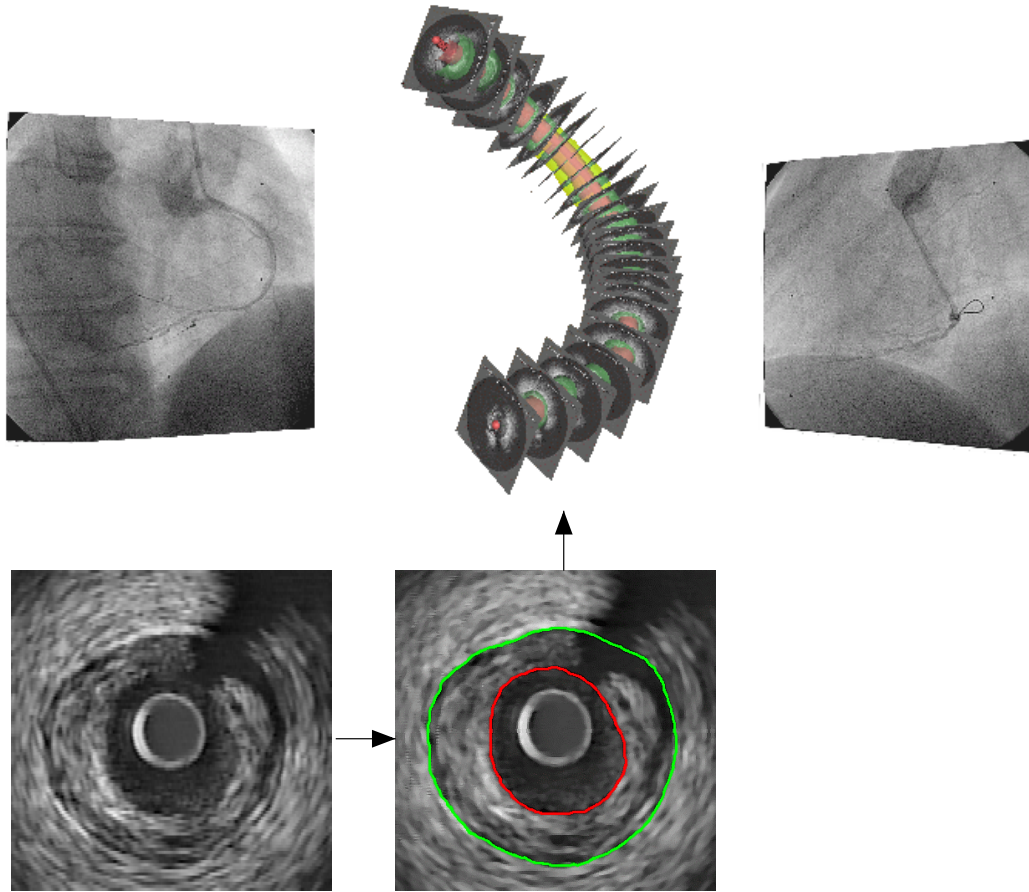
Fig. 1.   The fusion process: Angiograms of a stenosed human right coronary artery post intervention are shown in the background, from which the catheter path is reconstructed; IVUS pixel data and segmented contours (red luminal and green adventitial contours, see example frame) are mapped into 3-D space. Only a subset of the IVUS frames is shown here.
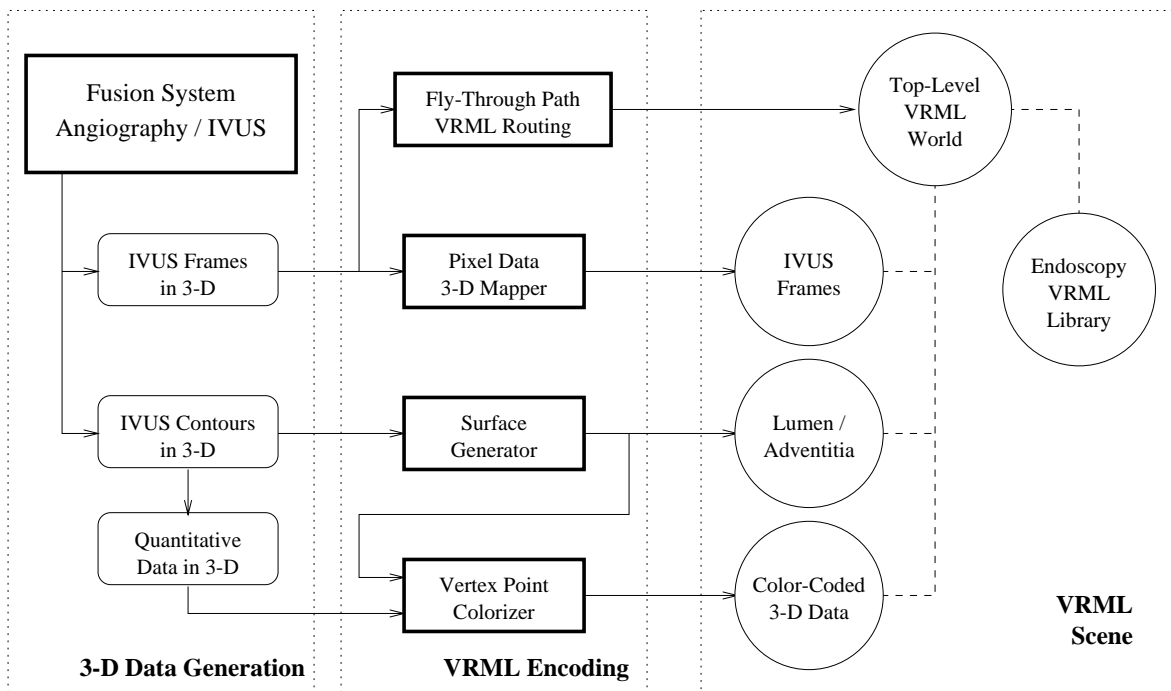

Fig. 2.   Processing scheme: 3-D IVUS pixel and contour data from the fusion system as well as quantitative results thereon are used to automatically create VRML objects, the fly-through trajectory, and control and routing definitions for VRML.

Angiography

Angiogram
Acquisition

ECG Sorting
by Heart Phase

Extraction of
Catheter / Lumen

3-D Trajectory
Reconstruction

Fusion

3-D Matching
of IVUS Frames

3-D Mapping
of Contours

Determination of
Absolute Orient.

Ultrasound

IVUS
Acquisition

ECG Sorting
by Heart Phase

Cross-Section
Segmentation

3-D Catheter Pullback Path
2-D to 3-D Mapping of Frames
3-D Lumen/Adventitia Contours

Fig. 3. Simplified flow chart of the fusion process: separate processing lines are followed for angiographic and IVUS data, then combined phase-wise in the fusion process; after determination of the absolute orientation and mapping of all contours into 3-D space, the 3-D/4-D model can be used for quantitative analysis and subsequent visualization.

Pullback

Stenosis

Observer
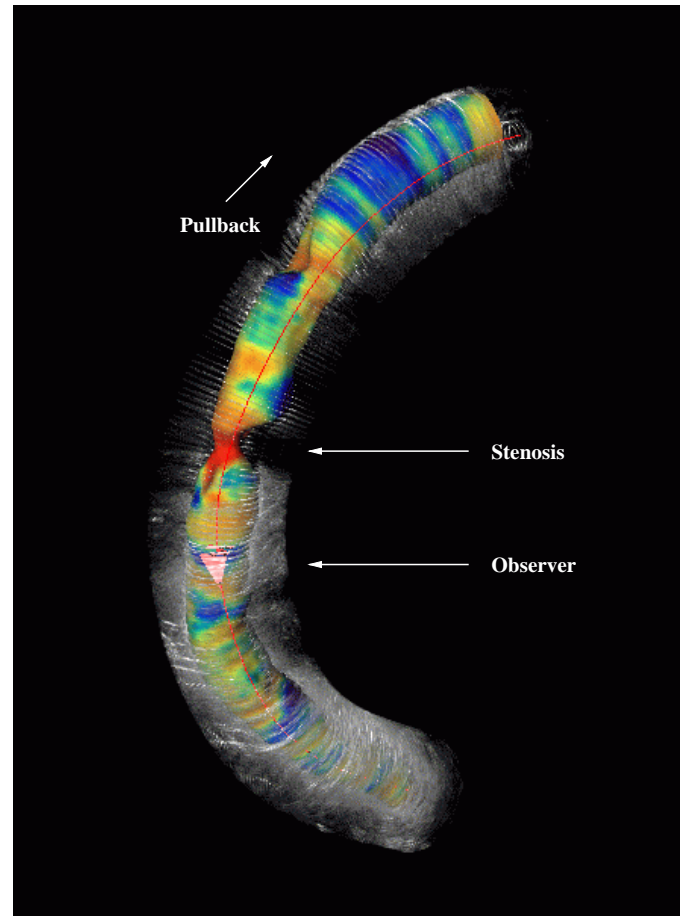
Fig. 4. Reconstructed right coronary artery pre intervention with results from computational hemodynamics (blue indicates low wall shear stress and red indicates high wall shear stress), fly-through trajectory based on catheter path, and endoscopic observer inserted.

(a)

(b)
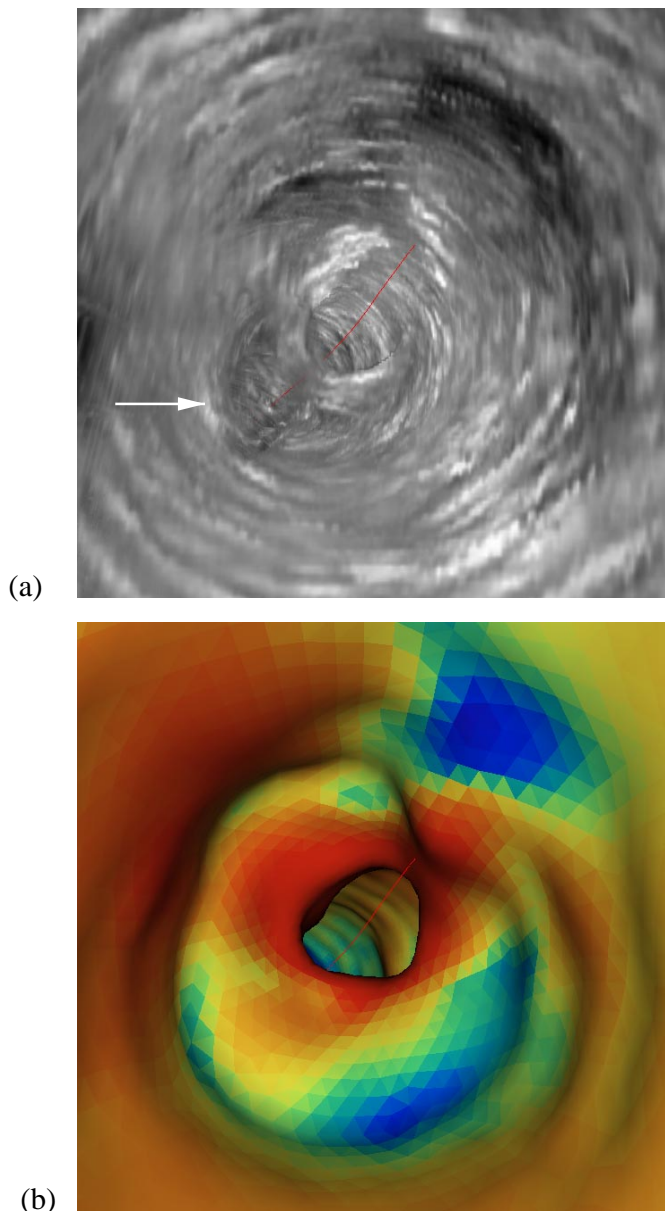
Fig. 5. Endoscopic view obtained from the virtual-observer location shown in Figure 4: (a) IVUS data in semi-transparent 3-D rendering, note that due to the shadowing in the IVUS data (arrow) it is actually possible to look behind the stenosis; (b) reconstructed lumen surface of the same view with color-coded local wall shear stress, showing the increase of shear stress in the stenotic area (red), while the segment distal to the stenosis has some turbulent flow with associated low shear stress (dark blue); the red line indicates the continuation of the fly-through trajectory.

(a)   (b)   (c)
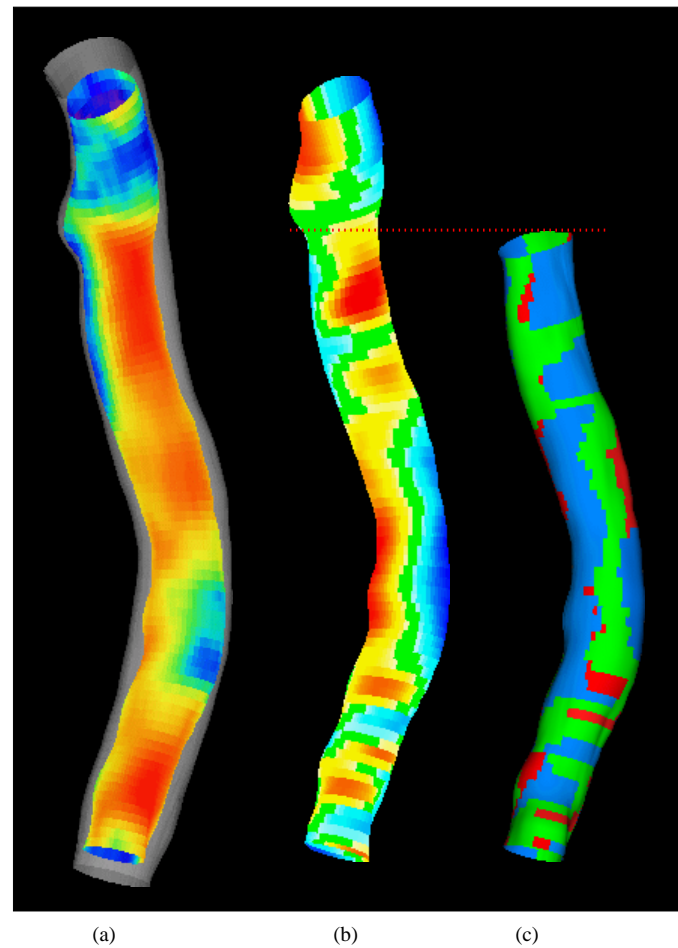
Fig. 6. Color-coding examples from the morphological study: (a) plaque thickness with a rainbow colormap from low (blue) to high (red) amounts of plaque and the adventitial border inserted; (b) local curvature, where red indicates "inner" curvature and blue indicates "outer" curvature, and green marks the sides; (c) higher-level analyses, where blue regions indicate a high correlation between local vessel curvature and circumferential plaque distribution. The image shows a left coronary artery with part of the left main and a segment of the left anterior descending artery; the branch to the left circumflex artery (red line) has not been followed and was discarded in (c).
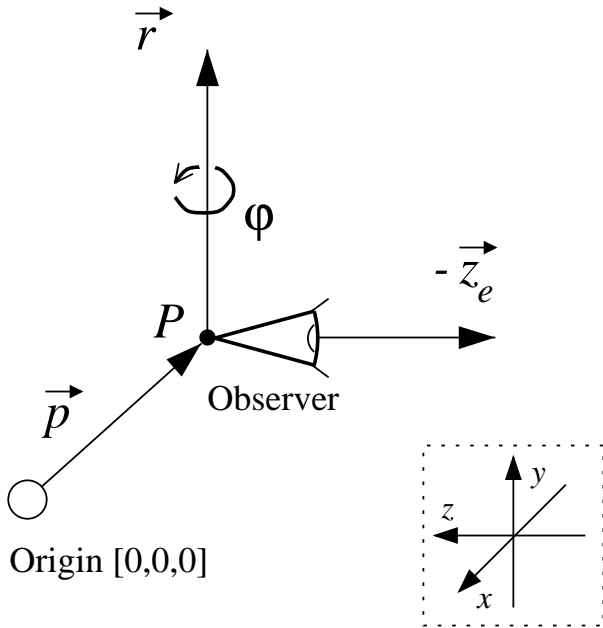
Fig. 7. Definition of a viewpoint as a triplet of $(\vec{p}, \vec{r}, \varphi)$ in VRML; the default viewing direction is along the negative z-axis.
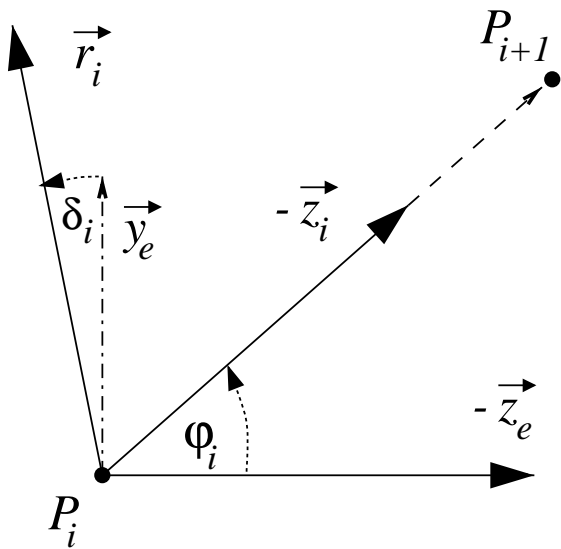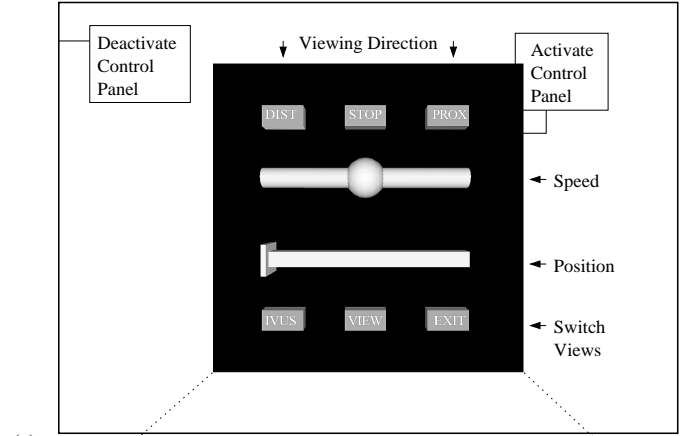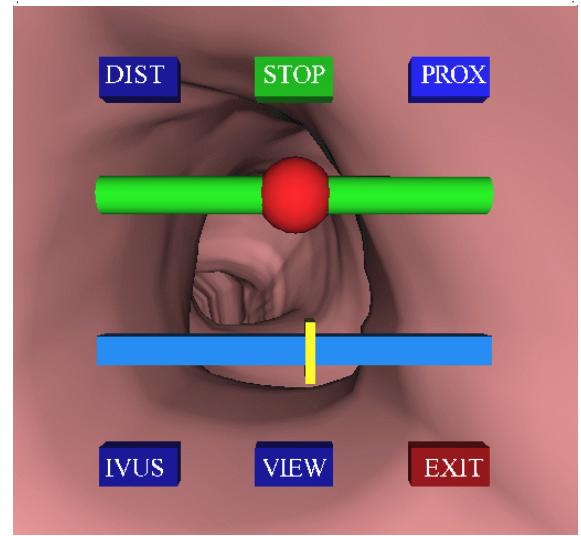

(a)

(b)

Fig. 9.   Appearance of the control panel when invoked: (a) the user can activate the control panel by clicking into the center of the image; afterwards, the controls remain active until the mouse leaves the black area and include buttons for viewing orientation and vessel representation, as well as sliders to navigate manually or automatically; (b) enlarged and cropped visualization of the panel in an actual endoscopic scene.

Fig. 8.   Rotation of the default viewing axis $-\vec{z}_e$ around $\vec{r}_i$ by φ_i to obtain the desired view $-\vec{z}_i$ from point P_i to P_{i+1} of the fly-through trajectory; $\vec{r}_i$ is obtained by rotating the local y-axis $(\vec{y}_e)$ by δ within the x/y-plane.
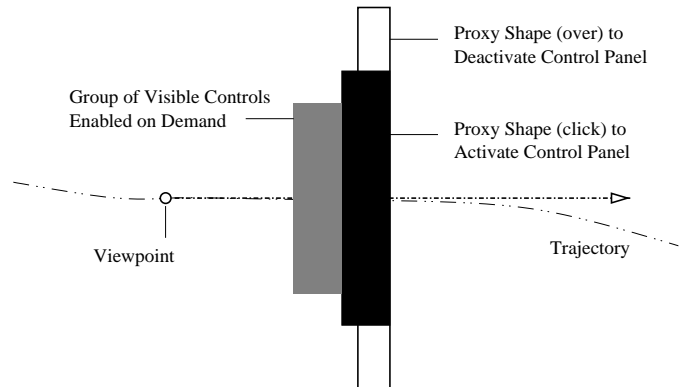

Fig. 10.   Realization of the control panel (side view): the panel moves with the viewpoint at a constant distance along the fly-through trajectory (dot-dot-dashed line); fully transparent proxy shapes are associated with touch sensors, thus allowing the user to enable or disable the visible control shapes located in the gray box, whereas the proxy shapes themselves remain invisible.
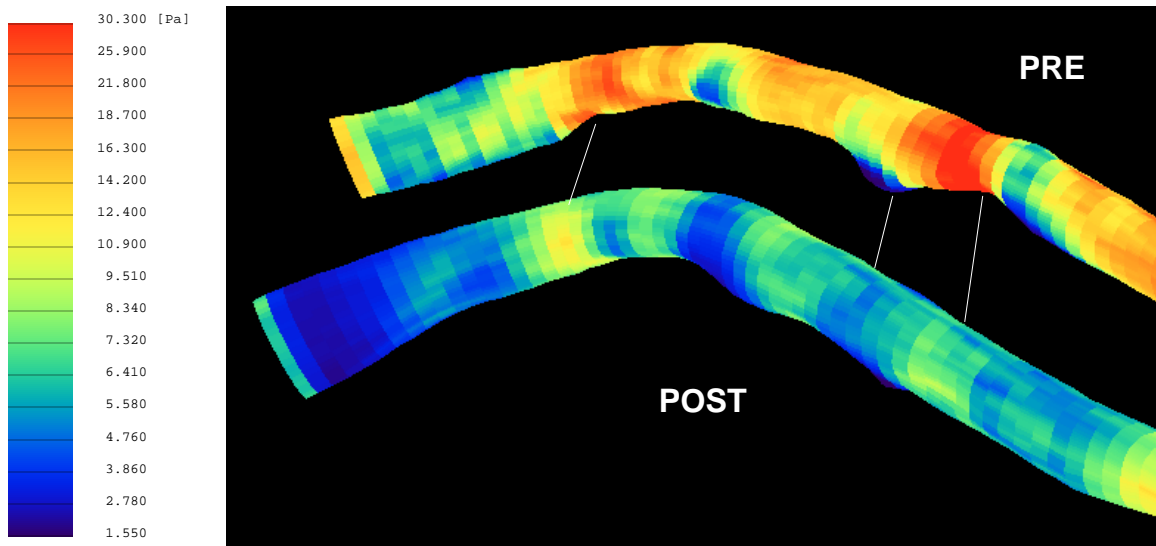
(a)
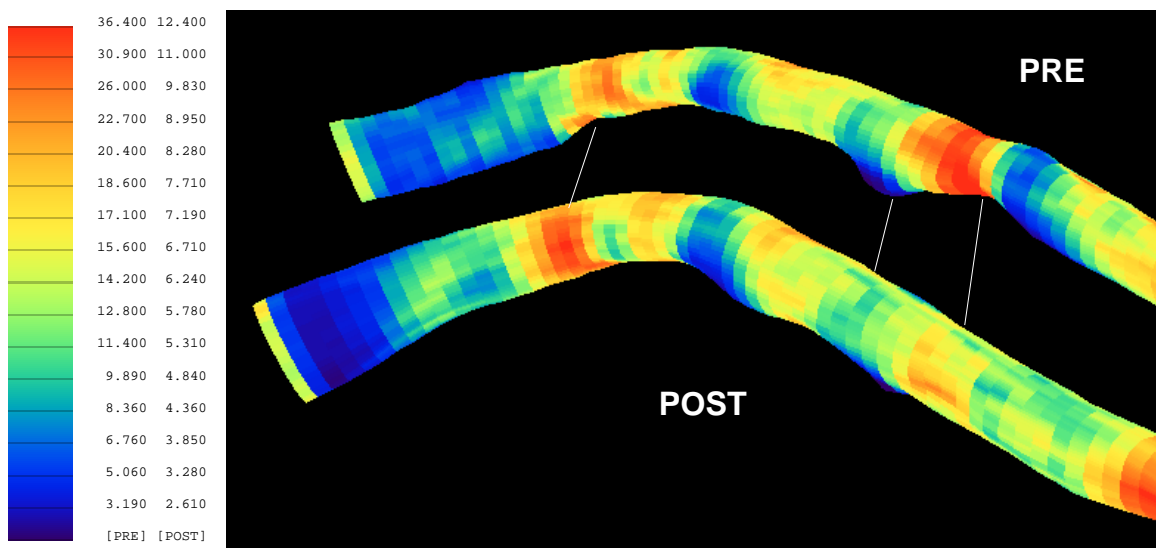
(b)

Fig. 11. Color coding of the wall shear stress in a left anterior descending artery: (a) a common mapping was used between the pre- and post-interventional analyses; it can clearly be seen that the lower blood pressure in the post-interventional state is reflected in the color scale — (b) the same hemodynamic analyses with the colormaps determined individually for each state; the differences in shear-stress distribution can now be compared more easily.
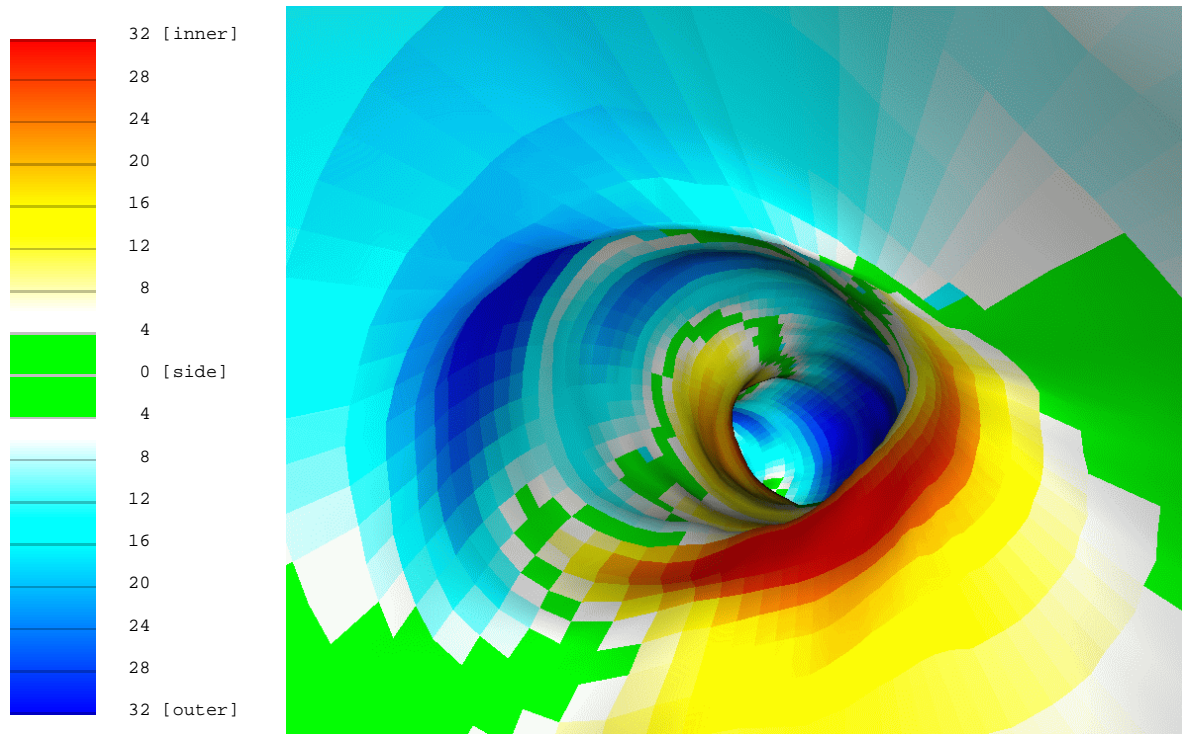
Fig. 12.   Endoscopic view with curvature information added as in Fig. 6(b), looking from the branching area (red line in Fig. 6) in distal direction; the inner curvature is indicated in red, the outer curvature in blue, and regions with a local curvature index of $|\kappa_{\mathrm{idx}}|{<}4°$/cm are marked in green (sides) – the tortuosity of the vessel can be better appreciated in this view as compared to the external view.